Enhancing exciton diffusion in monolayer WS_2 with *h*-BN bottom layer

Jang-Won Kang, Jin-Woo Jung, Taejin Lee, Jung Gon Kim, and Chang-Hee Cho *
Department of Emerging Materials Science, Daegu Gyeongbuk Institute of Science and Technology (DGIST), Daegu 42988, South Korea

(Received 11 January 2019; revised manuscript received 31 October 2019; published 21 November 2019)

We investigated two-dimensional (2D) exciton diffusion in monolayer WS_2 on both SiO_2 and hexagonal boron nitride (*h*-BN) layers to identify the exciton diffusion enhanced by the *h*-BN bottom layer using spatially resolved photoluminescence imaging combined with time-resolved spectroscopy. The WS_2 on the *h*-BN bottom layer shows an exciton diffusion coefficient of $38\,\mathrm{cm}^2/\mathrm{s}$, which is almost 1.7 times that of WS_2 on the SiO_2 layer. Electrostatic force microscopy confirms that the increase in the 2D exciton diffusion is mainly due to the reduction in the charge impurities and traps on the *h*-BN surface compared to the SiO_2 surface.

DOI: 10.1103/PhysRevB.100.205304

I. INTRODUCTION

Excitons in monolayers of semiconducting transition-metal dichalcogenides (TMDs) exhibit unique physical properties, such as extremely large exciton binding energy [1–3], charged excitons (trions) [4], and excitonic molecules (biexcitons) [5]. The abundance of interesting excitonic features facilitates the exploration of the novel quantum phenomena and new optoelectronic properties, including valley degrees of freedom [6–8], excitons with interlayer interactions [9], exciton-polaritons [10], and exciton Hall effects [11]. Moreover, stacked two-dimensional (2D) crystals, called van der Waals heterostructures [12], open the possibility of designing exciton properties and manipulating a variety of excitonic effects by using multiple combinations of 2D crystals [13]. However, the exciton properties in monolayer TMDs can be significantly altered by their surrounding environments, such as strain, substrate effect, and surrounding dielectrics [14–16]. Thus, a fundamental understanding of exciton properties in 2D heterostructures is of key importance for realizing the future applications of these novel materials.

Recently, the exciton dynamics and many-body interactions in the monolayer limit have been studied extensively to investigate excitonic diffusion and exciton-exciton annihilation for individual TMDs [17–22]. To understand the exciton properties in various layered heterostructures, a more systematic study on exciton transport is required, especially in terms of the effect of heterostructures. On the other hand, the electron transport properties of atomic-layered materials, such as graphene [23] and monolayer TMDs [24], are known to be greatly affected by the charge impurities and puddles on the surface of the SiO_2 substrate. In this regard, the use of a hexagonal boron nitride (*h*-BN) substrate, which is relatively free of charge impurities and traps and has an atomically smooth surface, significantly increases the electron mobility [23–26]. Also, it has been known that the optical properties in monolayer transition-metal dichalcogenides are greatly affected by the substrate, leading to the substrate-induced change in PL and Raman peak wavelength and intensity [16]. However, the exciton transport properties, particularly those in the TMD/*h*-BN layer, which can potentially provide an ideal testbed to study intrinsic exciton properties such as valley exciton and polariton physics, are largely unexplored.

Here, we report the 2D exciton diffusion in monolayer tungsten disulfide (WS_2) crystals on different bottom layers of SiO_2 and monolayer *h*-BN. The monolayer WS_2 crystals used in our experiments serve as a good material to investigate 2D excitonic phenomena because they have a higher photoluminescence (PL) quantum yield ($\sim$6%) than other 2D TMDs ($\sim$0.1% in monolayer MoS_2) [17,27]. To investigate the 2D exciton diffusion in monolayer WS_2 with different bottom layers, we visualize the spatial distribution of exciton density by utilizing spectrally and spatially resolved PL imaging combined with time-resolved spectroscopy. We find that the exciton diffusion length in monolayer WS_2 is greatly increased by introducing the *h*-BN bottom layer. Furthermore, electrostatic force microscopy (EFM) reveals that the increase in exciton diffusion is mainly due to the reduction in the charge impurities and traps on the *h*-BN surface compared to the SiO_2 surface.

II. EXPERIMENTAL APPROACH

To study the exciton diffusion in 2D van der Waals heterostructures of monolayer TMD on *h*-BN, we used WS_2 and *h*-BN monolayers separately grown by chemical vapor deposition (CVD) methods. The monolayer WS_2 crystals were grown on a SiO_2/Si substrate by using Ar gas, and WO_3 and S powders [28]. To fabricate WS_2 on the *h*-BN bottom layer, monolayer *h*-BN grown on Cu foils was transferred onto SiO_2/Si substrates by a wet-etching process of the Cu layer. Then, to stack monolayer WS_2 onto the *h*-BN layer, the as-grown monolayer WS_2 crystals were transferred onto the *h*-BN layer by a successive procedure of wet-etching and wet-transfer processes. To remove the supporting polymer residues and bubbles, we have performed a postannealing process of the *h*-BN layer for 3 h at 350 °C. The same fabrication procedure was carried out to obtain control samples of WS_2 on SiO_2 layer structures. Note that the monolayer WS_2 crystals transferred onto SiO_2 and *h*-BN were taken from the same

*Corresponding author: chcho@dgist.ac.kr

 ©2019 American Physical Society

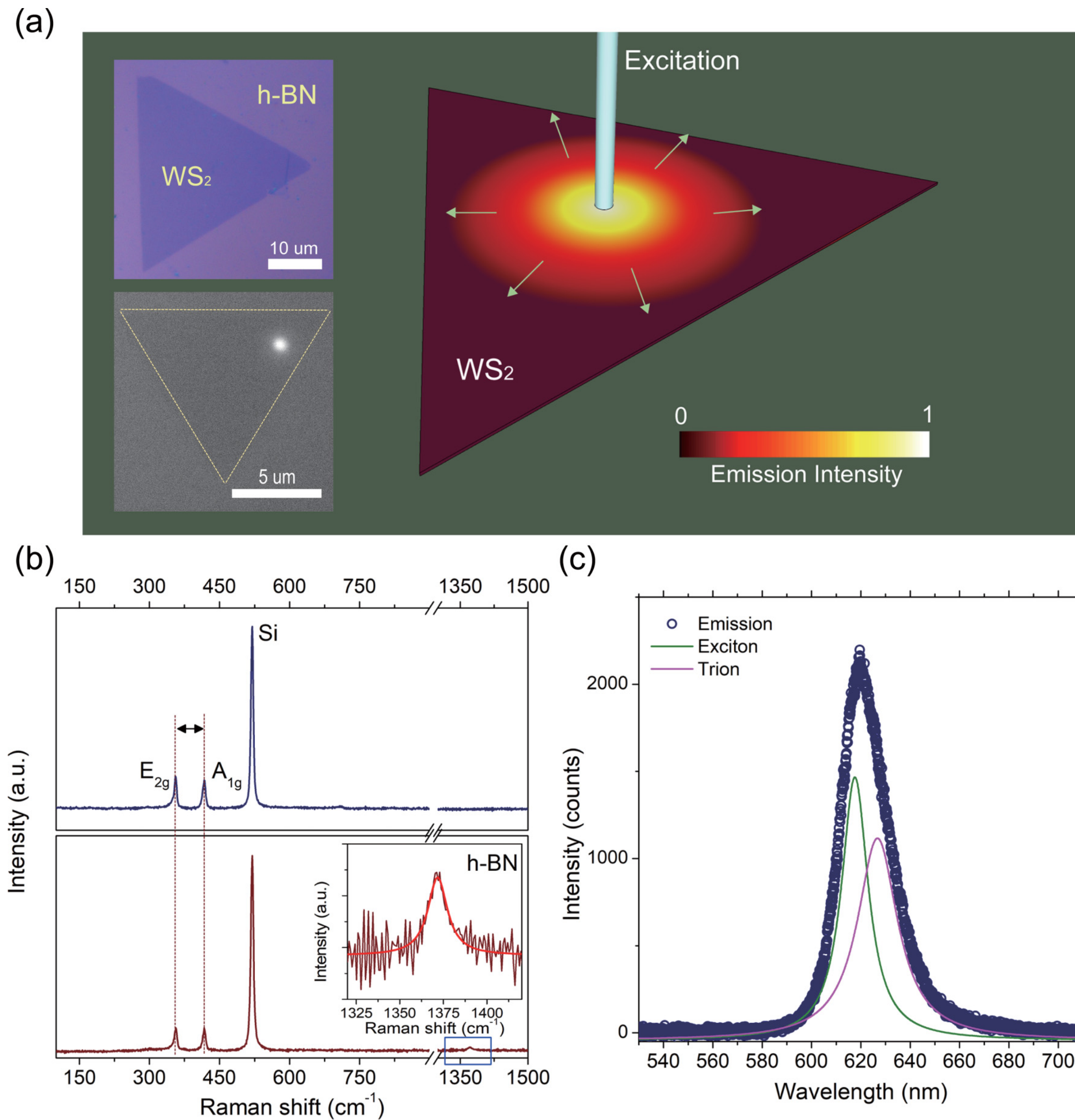

FIG. 1. (a) Schematic illustration of the 2D profile of emission intensity resulting from exciton diffusion in monolayer WS_2. The top inset shows an optical microscopy image of monolayer WS_2 transferred onto an *h*-BN layer. The bottom inset shows an emission image of monolayer WS_2 on the focal image plane of a micro-PL system. (b) Raman spectra of monolayer WS_2 on a SiO_2 layer (upper panel) and an *h*-BN layer (bottom panel), indicating that monolayer WS_2 was well transferred onto both the SiO_2 and *h*-BN layers. (c) Room-temperature PL spectra of monolayer WS_2, showing the strong light emission originating from the excitonic emission of the neutral excitons and trions in monolayer WS_2.

growth batch, and thus the quality of the samples on both SiO_2 and *h*-BN is nearly the same, allowing a systematic comparative study of the different bottom layers. Raman, steady-state PL, and time-resolved PL measurements were performed by employing a home-built confocal micro-PL setup. For all PL measurements, the excitation beam was focused using a 40× (NA = 0.6) objective, and the signal was collected with the same objective. As an excitation source, an argon-ion laser at 458 nm (continuous wave) and a picosecond pulsed laser with a wavelength of 454 nm and a repetition rate of 40 MHz were used to obtain steady-state and time-resolved PL data, respectively. To extract the diffusion length from the spatial profile of steady-state PL intensity, the diffusion equation was analytically calculated. EFM images were obtained using an atomic force microscopy (AFM) system in noncontact mode. All measurements were conducted under ambient conditions at room temperature.

III. RESULTS AND DISCUSSION

In monolayer WS_2, excitons generated at an excitation spot can be diffused in the plane of the 2D TMD due to the gradient of exciton density, subsequently leading to a spatial distribution of emission intensity due to radiative recombination processes of excitons at a finite distance, as shown in Fig. 1(a). Under continuous wave excitation, the spatial distribution of emission intensity can be treated as that of exciton density in a steady-state [29–31], enabling the direct visualization

of exciton diffusion phenomena via a 2D spatial map of PL spectra. To investigate the excitonic diffusion features depending on the interfacial layer (or substrate), monolayer WS_2 crystals grown by CVD were transferred onto SiO_2 and h-BN/SiO_2 substrates. The top inset of Fig. 1(a) shows an optical microscopy image of monolayer WS_2 crystals with a size of 30 μm transferred onto the h-BN layer, and the bottom inset of Fig. 1(a) presents a PL image of a monolayer WS_2 crystal, showing that the crystal size of monolayer WS_2 is much larger than the excitation spot size and is suitable for obtaining the 2D profile of PL spectra. Recently, it has been known that, in CVD-grown monolayer WS_2, the sulfur vacancy concentration near the edges of triangular crystals is much higher than that in the interior, leading to different PL features from the bound-excitons near the edges of monolayer crystals [32]. The diffusion and transport of excitons can be largely affected by the bound states at the edge of monolayer crystals. Thus, to avoid the exciton trapping, arising from the traps and defects at the edge of monolayer crystals, all PL measurements in our experiments have been performed on the interior region, at a distance of more than 5 μm from the edge of large monolayer crystals (>20 μm). Figure 1(b) shows that the Raman spectra of monolayer WS_2 transferred onto SiO_2 (upper panel) and h-BN (bottom panel) layers exhibit the characteristic Raman peaks of monolayer WS_2 (E_{2g} mode: 355.50 cm^{-1} and A_{1g} mode: 417.04 cm^{-1}) [33,34] with a peak separation of 61.54 cm^{-1} and a Raman peak of h-BN at 1370 cm^{-1} [35], indicating that monolayer WS_2 crystals were well transferred onto both the SiO_2 and h-BN layers. Figure 1(c) shows that the strong PL of monolayer WS_2 originates from the emission components of neutral and charged (trion) excitons centered at wavelengths of ~618 and ~628 nm, respectively [3]. The strong excitonic emission from monolayer WS_2 allows us to explore the exciton dynamics and transport properties at room temperature. Notably, we have observed a slight difference in the spectral shapes between WS_2 on SiO_2 and on h-BN. In the Supplemental Material [36], a comparison of normalized PL spectra shows the slight difference between WS_2 on SiO_2 and on h-BN. To this end, we have performed a double Lorentzian fit, allowing us to extract the individual exciton and trion components (see the Supplemental Material [36]). The fitting results were summarized in Table S1 of the Supplemental Material [36], showing a small redshift and broadening of both exciton and trion peaks in monolayer WS_2 on h-BN. Recent experimental observation showed that the appearance of redshift and broadening in the PL feature was attributed to local strain effects [37]. In the case of WS_2 on h-BN, the h-BN layer was transferred onto the SiO_2 substrate and subsequently the WS_2 layer was transferred onto the h-BN layer, while the WS_2 layer was transferred onto the flat SiO_2 substrate in the case of WS_2 on SiO_2. The transferred h-BN layer would have nanobubbles and wrinkles that can cause a local strain effect on the subsequently transferred WS_2 layer. We believe that the nanobubbles and wrinkles, which cause the local strain effect, are responsible for the small redshift and broadening of exciton peaks. The local strain might affect the exciton transport on the monolayer. Recent theoretical study has shown that the electron mobility in monolayer TMDs can be increased by a tensile strain [38], which is a similar situation with the presence of bubbles and wrinkles. Roughly, compared to WS_2 on SiO_2, the average local strain in WS_2 on h-BN is estimated to be about 0.1% by using a relation of 11.3 meV per % of strain for redshift of an A-exciton [37], indicating that the actual local strain is far below the range affecting the exciton transport in monolayer TMDs [39]. However, a detailed study of the local strain effect on the exciton diffusion length would be required to elucidate the transport mechanism with the nanobubbles and wrinkles.

To investigate the spatial profile of exciton density on monolayer WS_2, the PL intensity was mapped by scanning the image plane with an optical fiber using a piezo-positioning stage (see the Supplemental Material [36]), providing the advantage of a high spatial resolution of ~310 nm at a wavelength of about 620 nm, which is due to an enhanced pinhole effect caused by the out-of-focal-length configuration of the fiber mapping system (see the Supplemental Material [36]). Moreover, a distance calibration was carried out to obtain accurate spatial information on the image plane by measuring the intensity profile of end emissions along the long axis of CdS nanowires and comparing it with the real length of the nanowires (see the Supplemental Material [36]). Figure 2(a) presents the 2D profile (x-y plane) of the excitation laser spot measured on the SiO_2 surface, showing a nearly circular and symmetric shape with a Gaussian distribution with a diameter of ~1 μm, where the diameter is defined as the full width at $1/e^2$ of the maximum intensity value. In contrast to the excitation spot, the PL intensity profiles of monolayer WS_2 crystals exhibit a significant variation in size and shape due to exciton diffusion, as shown in Figs. 2(b) and 2(c). Importantly, an intriguing feature is observed in the 2D emission profiles of monolayer WS_2 crystals having a different bottom layer. The measurements clearly show that the size of the emission profile in monolayer WS_2 on the h-BN layer is much larger than that in monolayer WS_2 on the SiO_2 layer, indicating that the 2D exciton diffusion length in monolayer WS_2 is indeed increased by using the h-BN bottom layer, compared to the SiO_2 layer. It should be noted that, in monolayer WS_2, the lowest energy exciton species are the spin-forbidden dark excitons, which consist of an electron and a hole with an opposite spin in the same valley. Thus, the population exchange between the dark and bright states requires an electronic spin-flip process. As known in the study based on quantum dots, the spin-flip time is about 100 ns while the decay time of a bright exciton is below 1 ns [40], implying that the population exchange from a dark to a bright state is difficult to achieve within the fast decay time of the bright exciton. In addition, because the small energy difference (~11 meV) for the dark and bright states in a conduction band [41] would result in similar populations of the dark and bright states at room temperature, the PL signal would be dominated by the transition in the upper bright state, indicating that the population exchange gives a minor contribution to the spatial distribution of the PL signal. Due to these reasons, it is expected that the overall spatial PL distribution at room temperature is not significantly changed by the population exchange from the dark to bright excitons during the diffusion.

For quantitative analysis, the spectral intensity was extracted for one axis, e.g., the x-axis, by taking the PL

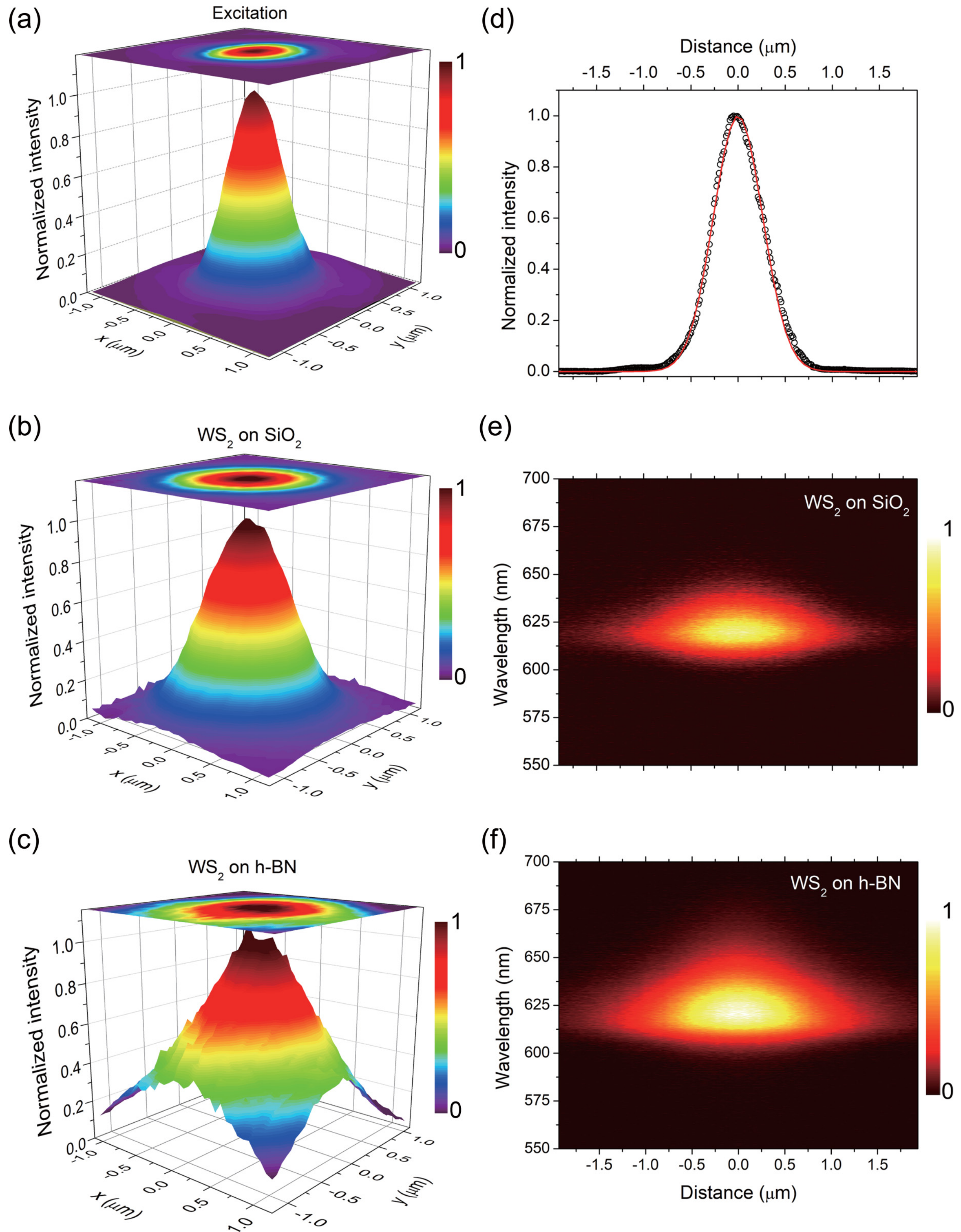

FIG. 2. (a) Intensity profile of the excitation spot with a Gaussian distribution. (b,c) PL intensity profiles in monolayer WS_2 on SiO_2 (b) and *h*-BN layers (c), showing that the intensity profile in WS_2 on the *h*-BN layer is much larger than that in WS_2 on the SiO_2 layer. All intensity profiles are circular and symmetric on the 2D *x*-*y* plane. (d) Intensity profile of the excitation laser spot with a Gaussian fit, corresponding to the Gaussian width of 0.37 μm. (e,f) Spatially and spectrally resolved PL maps from monolayer WS_2 on SiO_2 (e) and *h*-BN layers (f). The spatially and spectrally resolved PL maps show that the spatial profiles of PL intensity in monolayer WS_2 on both SiO_2 and *h*-BN are much larger than the excitation spot size, mainly due to the exciton diffusion on the 2D surface. All color plots were normalized by the maximum peak intensity at the center position.

spectra along the cross section of the 2D profile. Since the PL intensity profile as a function of distance (on the x-axis) is attributed to the spatial profile of diffused excitons, the exciton diffusion length can be calculated from the PL intensity profiles [29–31]. Figure 2(d) presents the 2D intensity profile of the excitation laser spot on the x-axis, showing a perfect Gaussian profile with a width of 0.37 μm. Note that the Gaussian fit for the excitation spot is given by $\Gamma(x) = \Gamma_0 \exp(-x^2/w^2)$, where Γ_0 is a proportionality constant and w is the width of the Gaussian distribution [30]. Spatially and spectrally resolved intensity profiles clearly reveal the increased spatial distribution in monolayer WS_2 crystals over the excitation spot due to the effect of exciton diffusion, as presented in Figs. 2(e) and 2(f). Also, the spectral shape in the monolayer WS_2 can be decomposed into two Lorentzian functions, allowing us to trace the exciton (~618 nm) and trion (~628 nm) emission depending on the collection position, corresponding to the exciton and the trion. The PL peak wavelength and linewidth of the exciton and trion emissions for both WS_2 on SiO_2 and on h-BN as a function of the collection position were investigated. The standard deviation for the PL peak wavelength and linewidth is below 1 nm over the collection position, indicating that the change over the collection position is negligible (see the Supplemental Material [36]). More importantly, the results directly demonstrate that the exciton and trion distribution is more extended in monolayer WS_2 on h-BN than in monolayer WS_2 on SiO_2. To understand the 2D excitonic diffusion processes with the different interfacial layers, we estimated the exciton and trion diffusion length from the measured emission intensity distribution on both the SiO_2 and h-BN layers, as shown in Figs. 3(a)–3(d). The spatial distribution of exciton density can be described by the 1D steady-state diffusion equation [30,31]:

$$D\frac{d^2n(x)}{dx^2} - \frac{n(x)}{\tau} - \gamma n^2(x) + \Gamma(x) = 0, \qquad (1)$$

where x is the position on WS_2, D is the diffusion coefficient along the x-axis, $n(x)$ is the exciton density, τ is the exciton lifetime, γ is the exciton-exciton annihilation rate, and $\Gamma(x)$ is the exciton generation rate. The exciton generation rate follows the laser intensity profile with a Gaussian shape, as shown in Fig. 2(d). Thus, the diffusion process in monolayer WS_2 can be described by the following equation:

$$L_D^2\frac{d^2n(x)}{dx^2} - n(x) - kn^2(x) + N\exp\left(-\frac{x^2}{w^2}\right) = 0, \qquad (2)$$

where $N = \Gamma_0\tau$ is a constant, $k = \gamma\tau$ is the annihilation rate constant, and $L_D = \sqrt{D\tau}$ is the diffusion length. This equation can be analytically solved to extract the diffusion length from the spatial profile of PL intensity. For the excitation range of $0.57-2.83\,\mathrm{kW/cm^2}$, the electron-hole pair density was estimated to be $(7.4\times10^{10})-(2.2\times10^{11})\,\mathrm{cm^{-2}}$ by considering an absorption cross section of $\sim4.8\times10^5\,\mathrm{cm^{-1}}$, a normal incidence reflectivity of ~0.55 on the WS_2 surface [42], and a calculated reflectivity (0.28) for the substrate interference effect (270-nm-thick SiO_2 on Si) at the excitation wavelength (see the Supplemental Material [36]), and exploiting a transfer-matrix method for absorbed power density in monolayer WS_2. The exciton radiative lifetime was measured to be 64 ps from time-resolved PL spectroscopy, as discussed later. Since the exciton diffusion in such a density regime can be affected by exciton-exciton annihilation processes [17,21], the diffusion length was obtained considering the annihilation term. To incorporate the annihilation rate into the calculation, we estimated the exciton-exciton annihilation rate (γ) by investigating the density-induced recombination rate [43], which was obtained from the time-resolved PL spectra measured at three different exciton densities (see the Supplemental Material [36]). The estimated exciton-exciton annihilation rates for monolayer WS_2 on SiO_2 and h-BN were 0.10 and $0.31\,\mathrm{cm^2/s}$, respectively, indicating that the estimated values are consistent with the reported exciton-exciton annihilation rate of monolayer WS_2 crystals ($0.11-0.41\,\mathrm{cm^2/s}$) [17,43,44]. Because the enhancement in exciton diffusion can increase the probability of exciton-exciton interaction [21,43], the higher exciton-exciton annihilation rate in WS_2 on h-BN than in WS_2 on SiO_2 is attributed to the enhanced exciton diffusion process on the h-BN bottom layer. For the measured spatial profiles of PL intensity, we performed least-squares fits with the diffusion equation to determine the values of the exciton diffusion length (L_D). The resulting diffusion length of monolayer WS_2 on SiO_2 lies in the range of 330–380 nm for excitons and 300–330 nm for trions with the varied excitation of $0.57-2.83\,\mathrm{kW/cm^2}$ [Figs. 3(a) and 3(b)], which is in good agreement with the values reported of exciton diffusion lengths for WS_2 and other TMDs (350–400 nm) [17–19]. Interestingly, compared to that of monolayer WS_2 on SiO_2, the diffusion length of monolayer WS_2 on h-BN is greatly increased to 450–500 nm for both the excitons and trions in the same excitation range [Figs. 3(c) and 3(d)], clearly indicating the enhancement in the diffusion length of both the exciton and trion on the h-BN layer. Note that the measurements of exciton diffusion lengths were carried out for three samples for each structure to reflect the sample-to-sample variation (see the Supplemental Material [36]). Figures 3(e) and 3(f) present the average diffusion lengths on the SiO_2 and h-BN layers for the excitation range of $0.57-2.83\,\mathrm{kW/cm^2}$, showing that both exciton and trion diffusion lengths are increased in monolayer WS_2 on the h-BN layer compared to that on the SiO_2 layer. The results also show that the exciton and trion diffusion lengths in WS_2 on the h-BN layer are almost the same at each excitation power density, while in WS_2 on the SiO_2 layer, the diffusion length of trions is slightly shorter than that of excitons. These results imply that the diffusion of charged species (i.e., trions) is more affected by the charge impurities on the substrate surface. As discussed above, the direct visualization of the exciton density profile clearly indicates that the exciton diffusion length in monolayer WS_2 crystals is greatly enhanced by ~22% with the h-BN interfacial layer compared to the SiO_2 layer. In addition, to check the diffusion length of as-grown WS_2 without any transfer processes, we have measured the spatially resolved PL spectrum (see the Supplemental Material [36]). The spectral shape of as-grown WS_2 corresponds to a single Lorentzian function centered at a wavelength of 630 nm, while the transferred WS_2 is composed of a double Lorentzian function centered at ~618 and ~630 nm. Although the same SiO_2/Si substrate has been employed for as-grown and transferred samples, the neu-

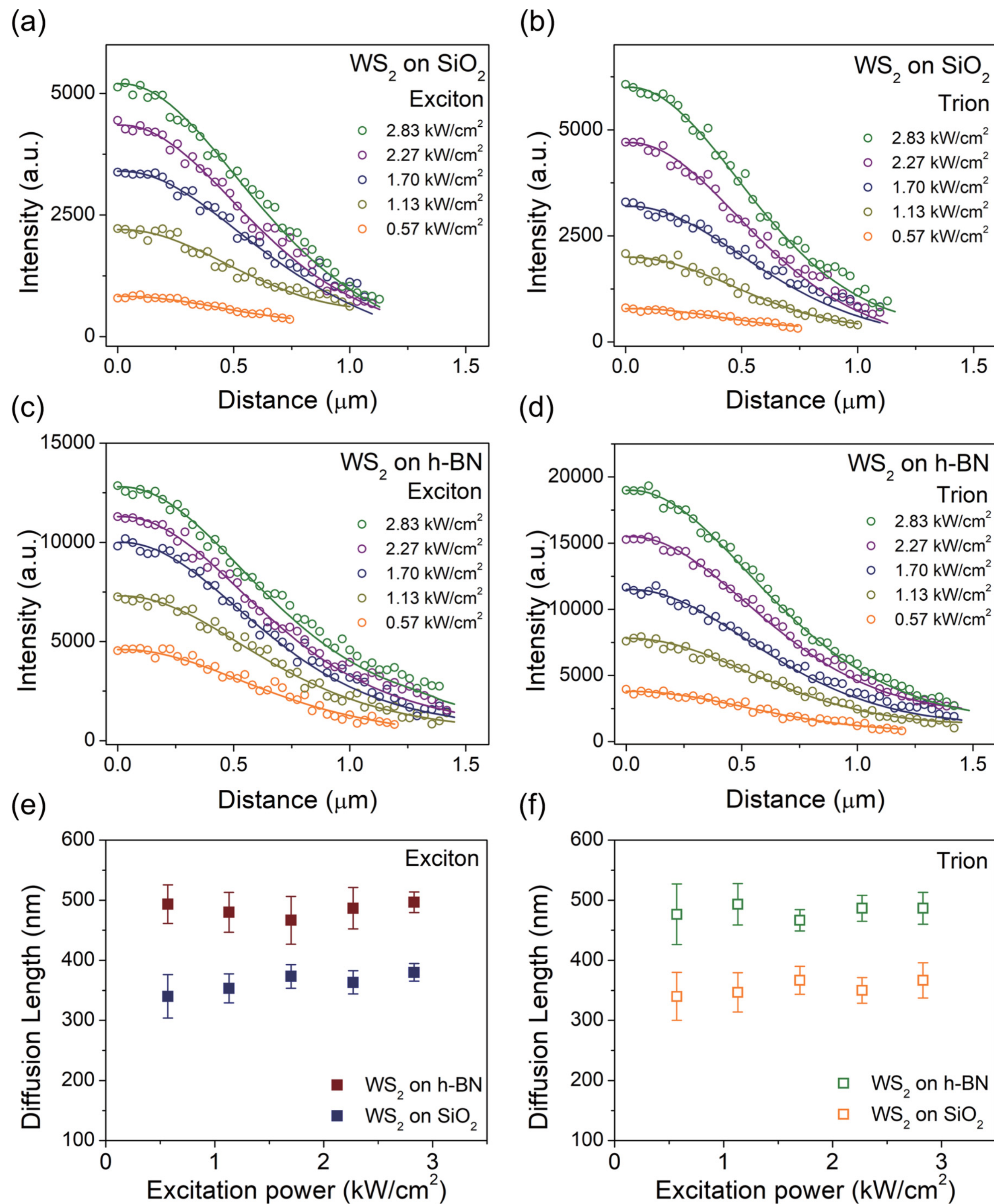

FIG. 3. (a)–(d) Spatial distribution of PL intensity resulting from the exciton and trion diffusion in monolayer WS_2 on the SiO_2 (a,b) and *h*-BN (c,d) layers. The colored lines indicate a best fit obtained from the analytical calculation of the 1D steady-state diffusion equation. (e,f) Averaged exciton (e) and trion (f) diffusion length in monolayer WS_2 on SiO_2 and *h*-BN for a total of three samples.

tral exciton emission at ∼618 nm was only observed in the transferred samples. The appearance of neutral exciton emission in the transferred samples would indicate that unintentional contamination and residues from seed promoters during the CVD growth process can be effectively reduced by wet-transfer processes. Also, we have estimated the diffusion length of as-grown monolayer WS_2 without transfer processes (see the Supplemental Material [36]). The estimated diffusion length for as-grown WS_2 is about 340–420 nm, which is quite similar to the diffusion length in the transferred WS_2. Thus, these results indicate that the significant degradation of WS_2 is not caused by the wet-transfer processes.

Recent time-resolved PL experiments on monolayer TMDs revealed that the exciton decay dynamics are significantly affected by density-induced many-body effects, underlining that the exciton-exciton annihilation, often identified as Auger

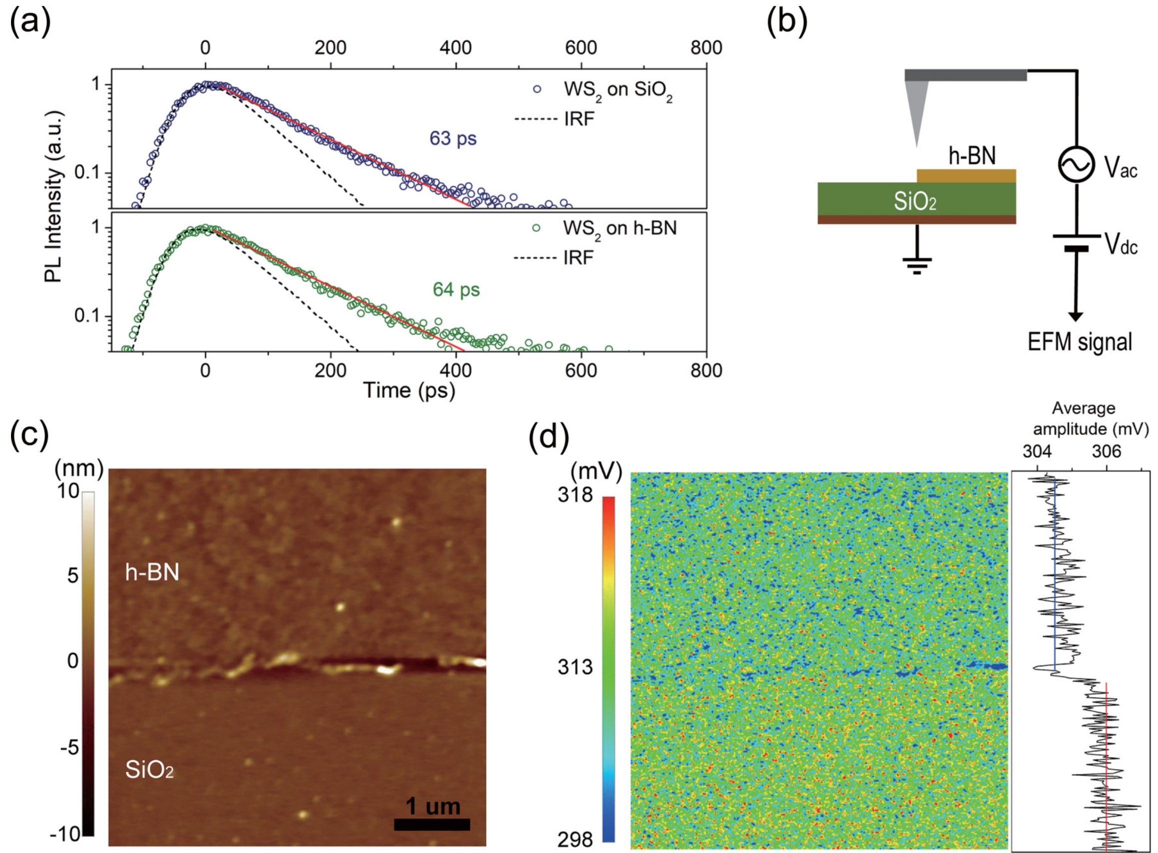

FIG. 4. (a) Time-resolved PL spectrum measured at the emission center for WS_2 on SiO_2 (top) and *h*-BN (bottom). The PL decay data were obtained under pulsed excitation with a pumping energy of $30\,\mathrm{nJ/cm^2}$. The PL decay signal was fitted by a single exponential function. (b) Schematic illustration of the EFM system, where V_{dc} is the dc bias applied to the tip and V_{ac} is the ac bias with a resonance frequency of ω for the deflection of the cantilever. The EFM signal can be detected by resolving the electrostatic contribution to the frequency ω. (c) AFM topographic image of the SiO_2 substrate partially covered by the *h*-BN layer. (d) EFM amplitude on the SiO_2 substrate partially covered with the *h*-BN layer when a dc bias of −6 V was applied to the tip, showing that the EFM amplitude on the *h*-BN region is relatively lower than that on the SiO_2 layer. The right panel displays the average value of the EFM amplitude along the vertical direction, showing the distinct EFM amplitudes in both areas of *h*-BN and the SiO_2 layer.

recombination, is an important nonradiative recombination channel at the high-density regime [45]. For monolayer TMDs, the PL decay time is drastically decreased with increasing exciton density by the Auger-type exciton-exciton annihilation process, leading to a more rapid decrease in PL intensity in the time domain [17,21,43]. In our monolayer WS_2 crystals, we observed a decrease in PL decay time at exciton densities above $\sim 3 \times 10^{10}\,\mathrm{cm^{-2}}$ (see the Supplemental Material [36]). Thus, to obtain the exciton decay time while avoiding the exciton-exciton annihilation process, the time-resolved PL decay was measured under low excitation with a pumping energy of $\sim 30\,\mathrm{nJ/cm^2}$, corresponding to an exciton density of approximately $1.0 \times 10^{10}\,\mathrm{cm^{-2}}$. In Fig. 4(a), the PL decay signals for WS_2 on both SiO_2 and *h*-BN were fitted by a single exponential function considering the instrumental response function (IRF) (see the Supplemental Material [36]). In such a low excitation power regime, the exciton lifetime on SiO_2 and *h*-BN was estimated to be 63 and 64 ps, respectively, indicating that the timescales for recombination processes in the WS_2 monolayers on both SiO_2 and *h*-BN layers are quite similar. As a rough estimation ($L_D = \sqrt{D\tau}$) using the measured exciton lifetime, the exciton diffusion coefficients (D) are estimated to be $\sim 38\,\mathrm{cm^2/s}$ for WS_2 on *h*-BN and $\sim 22\,\mathrm{cm^2/s}$ for WS_2 on SiO_2 in the low exciton density regime, which reinforces that the *h*-BN layer enhances the 2D exciton diffusion of monolayer WS_2 crystals by a factor of ∼1.7. These results clearly imply that the *h*-BN bottom layer can be a good substrate to observe the intrinsic properties of exciton diffusion in atomically thin 2D semiconductors.

To investigate the surface charge states on both the *h*-BN and SiO_2 layers, we performed EFM measurements on a SiO_2 layer partially covered by an *h*-BN layer. The EFM measurement is based on noncontact mode AFM, in which surface electrostatic interactions between a sample and an AFM tip are detected. As shown in Fig. 4(b), the total applied voltage (V) between the tip and the sample can be expressed by the relation $V = V_{\mathrm{dc}} - V_s + V_{\mathrm{ac}}\cos\omega t$, where V_{dc} is the dc bias applied to the tip, V_s is the surface potential of the sample, and V_{ac} is the ac bias additively applied to the tip. Then, the relationship between the electrostatic force (F) and the applied voltage is given by [46]

$$\mathrm{F} = \frac{1}{2}\frac{\partial C}{\partial z}(V_{\mathrm{dc}} - V_s + V_{\mathrm{ac}}\cos\omega t)^2, \tag{3}$$

where C is the tip-sample capacitance at a tip-sample distance of z. By expanding the right side of the above equation and taking the first harmonic component ($\cos \omega t$ term), the electrostatic force to the frequency ω is simplified as $F = (\partial C/\partial z)(V_{dc} - V_s)V_{ac}\cos\omega t$ [47]. In our EFM measurements, a dc bias (V_{dc}) of -6 V was applied to obtain a high contrast of the EFM signal from the insulating layers. When the V_{ac} ($\sim$2 V) of the oscillation frequency ($\omega \sim 17$ kHz) was applied to the tip, the oscillation amplitude could be modulated by the electrostatic contribution ($V_{dc} - V_s$) at the oscillation frequency ω, enabling us to acquire the EFM signal contrast on the sample surface. Note that this electrostatic signal does not provide quantitative information because the signal is detected in noncontact mode, but it does allow a qualitative comparison of electrostatic interactions for different surface charge states. Figure 4(c) shows the topographic image of the h-BN layer on the SiO_2 substrate, showing that the h-BN layer is partially covering the SiO_2 substrate. While local cracks are observed near the edge of the h-BN layer, the boundary between the h-BN and the SiO_2 layers is clearly distinguished, as shown in Fig. 4(c). Figure 4(d) shows the measured EFM amplitude on both the h-BN and the SiO_2 surfaces. Comparison with the topographic image in Fig. 4(c) indicates that the region with a high EFM amplitude is well matched with the SiO_2 surface area. In our measurements with a fixed dc bias of the tip, the EFM amplitude is proportional to the surface potential induced by surface charges and thus identifies the difference in the surface potentials between the h-BN and the SiO_2 layers. Therefore, the relatively lower EFM amplitude on the h-BN layer clearly indicates that compared to the surface of the SiO_2 substrate, the h-BN layer is relatively free of charged impurities and traps due to the complete chemical bonds in the in-plane direction [26,33]. These results emphasize that the exciton diffusion and transport in 2D monolayer semiconductors are greatly altered by charged impurities and traps on the bottom layer and can be tailored by designing van der Waals heterostructures.

IV. CONCLUSIONS

In conclusion, we systematically investigated the 2D exciton diffusion in two different layered structures, namely WS_2/h-BN and WS_2/SiO_2. From the direct visualization of the exciton distribution combined with time-resolved spectroscopy and analytical calculations, we found that the 2D diffusion coefficient of the WS_2/h-BN layer is approximately 38 cm^2/s, which is 1.7 times larger than that (22 cm^2/s) of WS_2 on the SiO_2 layer. Furthermore, the EFM measurements revealed that the increase in the exciton diffusion is mainly due to the reduction in the charge impurities and traps on the h-BN surface compared to the SiO_2 surface. Our work suggests that elaborately designed 2D heterostructures are greatly needed to obtain the intrinsic 2D exciton properties for both the exploration of intriguing physics in ultrathin semiconductors and application to future devices. In particular, in the device applications related to the valley Hall effect and valley excitons utilizing the photocurrent and Hall voltage generated by circularly polarized light [48,49], the device structures including contact separations might be strongly affected by the exciton diffusion length. In this regard, our results can provide an important idea to design the device geometry.

ACKNOWLEDGMENTS

This work was supported by the Basic Science Research Program (2016R1A2B4014448, 2016R1A6A3A11933287, and 2019R1A2C1088525) through the National Research Foundation of Korea, and by the DGIST R&D Program (19-BD-0401) funded by the Ministry of Science and ICT of the Korean Government.

[1] M. M. Ugeda, A. J. Bradley, S. F. Shi, F. H. Da Jornada, Y. Zhang, D. Y. Qiu, W. Ruan, S. K. Mo, Z. Hussain, Z. X. Shen, F. Wang, S. G. Louie, and M. F. Crommie, Nat. Mater. **13**, 1091 (2014).

[2] A. Chernikov, T. C. Berkelbach, H. M. Hill, A. Rigosi, Y. Li, O. B. Aslan, D. R. Reichman, M. S. Hybertsen, and T. F. Heinz, Phys. Rev. Lett. **113**, 076802 (2014).

[3] B. Zhu, X. Chen, and X. Cui, Sci. Rep. **5**, 9218 (2015).

[4] K. F. Mak, K. He, C. Lee, G. H. Lee, J. Hone, T. F. Heinz, and J. Shan, Nat. Mater. **12**, 207 (2013).

[5] Y. You, X.-X. Zhang, T. C. Berkelbach, M. S. Hybertsen, D. R. Reichman, and T. F. Heinz, Nat. Phys. **11**, 477 (2015).

[6] X. Xu, W. Yao, D. Xiao, and T. F. Heinz, Nat. Phys. **10**, 343 (2014).

[7] K. F. Mak, K. He, J. Shan, and T. F. Heinz, Nat. Nanotechnol. **7**, 494 (2012).

[8] H. Zeng, J. Dai, W. Yao, D. Xiao, and X. Cui, Nat. Nanotechnol. **7**, 490 (2012).

[9] J. G. Kim, W. S. Yun, S. Jo, J. Lee, and C.-H. Cho, Sci. Rep. **6**, 29813 (2016).

[10] X. Liu, T. Galfsky, Z. Sun, F. Xia, E. Lin, Y.-H. Lee, S. Kéna-Cohen, and V. M. Menon, Nat. Photon. **9**, 30 (2015).

[11] M. Onga, Y. Zhang, T. Ideue, and Y. Iwasa, Nat. Mater. **16**, 1193 (2017).

[12] A. K. Geim and I. V Grigorieva, Nature (London) **499**, 419 (2013).

[13] P. Rivera, J. R. Schaibley, A. M. Jones, J. S. Ross, S. Wu, G. Aivazian, P. Klement, K. Seyler, G. Clark, N. J. Ghimire, J. Yan, D. G. Mandrus, W. Yao, and X. Xu, Nat. Commun. **6**, 6242 (2015).

[14] I. Niehues, R. Schmidt, M. Drüppel, P. Marauhn, D. Christiansen, M. Selig, G. Berghäuser, D. Wigger, R. Schneider, L. Braasch, R. Koch, A. Castellanos-Gomez, T. Kuhn, A. Knorr, E. Malic, M. Rohlfing, S. Michaelis de Vasconcellos, and R. Bratschitsch, Nano Lett. **18**, 1751 (2018).

[15] Y. Lin, X. Ling, L. Yu, S. Huang, A. L. Hsu, Y.-H. Lee, J. Kong, M. S. Dresselhaus, and T. Palacios, Nano Lett. **14**, 5569 (2014).

[16] M. Buscema, G. A. Steele, H. S. J. van der Zant, and A. Castellanos-Gomez, Nano Res. **7**, 561 (2014).

[17] L. Yuan and L. Huang, Nanoscale **7**, 7402 (2015).
[18] N. Kumar, Q. Cui, F. Ceballos, D. He, Y. Wang, and H. Zhao, Nanoscale **6**, 4915 (2014).
[19] J. He, D. He, Y. Wang, Q. Cui, F. Ceballos, and H. Zhao, Nanoscale **7**, 9526 (2015).
[20] D. Sun, Y. Rao, G. A. Reider, G. Chen, Y. You, L. Brézin, A. R. Harutyunyan, and T. F. Heinz, Nano Lett. **14**, 5625 (2014).
[21] S. Mouri, Y. Miyauchi, M. Toh, W. Zhao, G. Eda, and K. Matsuda, Phys. Rev. B **90**, 155449 (2014).
[22] N. Kumar, Q. Cui, F. Ceballos, D. He, Y. Wang, and H. Zhao, Phys. Rev. B **89**, 125427 (2014).
[23] C. R. Dean, A. F. Young, I. Meric, C. Lee, L. Wang, S. Sorgenfrei, K. Watanabe, T. Taniguchi, P. Kim, K. L. Shepard, and J. Hone, Nat. Nanotechnol. **5**, 722 (2010).
[24] X. Cui, G.-H. Lee, Y. D. Kim, G. Arefe, P. Y. Huang, C.-H. Lee, D. A. Chenet, X. Zhang, L. Wang, F. Ye, F. Pizzocchero, B. S. Jessen, K. Watanabe, T. Taniguchi, D. A. Muller, T. Low, P. Kim, and J. Hone, Nat. Nanotechnol. **10**, 534 (2015).
[25] S. Ghatak, A. N. Pal, and A. Ghosh, ACS Nano **5**, 7707 (2011).
[26] M. W. Iqbal, M. Z. Iqbal, M. F. Khan, M. A. Shehzad, Y. Seo, J. H. Park, C. Hwang, and J. Eom, Sci. Rep. **5**, 10699 (2015).
[27] C. Cong, J. Shang, Y. Wang, and T. Yu, Adv. Opt. Mater. **6**, 1700767 (2018).
[28] S. Jo, J. W. Jung, J. Baik, J. W. Kang, I. K. Park, T. S. Bae, H. S. Chung, and C. H. Cho, Nanoscale **11**, 8706 (2019).
[29] F. Cadiz, C. Robert, E. Courtade, M. Manca, L. Martinelli, T. Taniguchi, K. Watanabe, T. Amand, A. C. H. Rowe, D. Paget, B. Urbaszek, and X. Marie, Appl. Phys. Lett. **112**, 152106 (2018).
[30] S. Moritsubo, T. Murai, T. Shimada, Y. Murakami, S. Chiashi, S. Maruyama, and Y. K. Kato, Phys. Rev. Lett. **104**, 247402 (2010).
[31] P. Irkhin and I. Biaggio, Phys. Rev. Lett. **107**, 017402 (2011).
[32] V. Carozo, Y. Wang, K. Fujisawa, B. R. Carvalho, A. McCreary, S. Feng, Z. Lin, C. Zhou, N. Perea-López, A. L. Elías, B. Kabius, V. H. Crespi, and M. Terrones, Sci. Adv. **3**, e1602813 (2017).
[33] A. Molina-Sánchez and L. Wirtz, Phys. Rev. B **84**, 155413 (2011).
[34] A. Berkdemir, H. R. Gutiérrez, A. R. Botello-Méndez, N. Perea-López, A. L. Elías, C.-I. Chia, B. Wang, V. H. Crespi, F. López-Urías, J.-C. Charlier, H. Terrones, and M. Terrones, Sci. Rep. **3**, 1755 (2013).
[35] L. H. Li, E. J. G. Santos, T. Xing, E. Cappelluti, R. Roldán, Y. Chen, K. Watanabe, and T. Taniguchi, Nano Lett. **15**, 218 (2015).
[36] See Supplemental Material at http://link.aps.org/supplemental/10.1103/PhysRevB.100.205304 for further information about the experimental observation and a detailed description of the experimental approach.
[37] Y. Wang, C. Cong, W. Yang, J. Shang, N. Peimyoo, Y. Chen, J. Kang, J. Wang, and W. Huang, Nano Res. **8**, 2562 (2015).
[38] M. Hosseini, M. Elahi, M. Pourfath, and D. Esseni, IEEE Trans. Electron Dev. **62**, 3192 (2015).
[39] D. F. C. Leon, Zi. Li, S. W. Jang, C.-H. Cheng, and P. B. Deotare, Appl. Phys. Lett. **113**, 252101 (2018).
[40] J. Johansen, B. Julsgaard, S. Stobbe, J. M. Hvam, and P. Lodahl, Phys. Rev. B **81**, 081304(R) (2010).
[41] J. P. Echeverry, B. Urbaszek, T. Amand, X. Marie, and I. C. Gerber, Phys. Rev. B **93**, 121107(R) (2016).
[42] H.-L. Liu, C.-C. Shen, S.-H. Su, C.-L. Hsu, M.-Y. Li, and L.-J. Li, Appl. Phys. Lett. **105**, 201905 (2014).
[43] M. Kulig, J. Zipfel, P. Nagler, S. Blanter, C. Schüller, T. Korn, N. Paradiso, M. M. Glazov, and A. Chernikov, Phys. Rev. Lett. **120**, 207401 (2018).
[44] Y. Hoshi, T. Kuroda, M. Okada, R. Moriya, S. Masubuchi, K. Watanabe, T. Taniguchi, R. Kitaura, and T. Machida, Phys. Rev. B **95**, 241403(R) (2017).
[45] G. Moody, J. Schaibley, and X. Xu, J. Opt. Soc. Am. B **33**, C39 (2016).
[46] A. Castellanos-Gomez, E. Cappelluti, R. Roldán, N. Agraït, F. Guinea, and G. Rubio-Bollinger, Adv. Mater. **25**, 899 (2013).
[47] J. W. Hong, S. I. Park, and Z. G. Khim, Rev. Sci. Instrum. **70**, 1735 (1999).
[48] N. Ubrig, S. Jo, M. Philippi, D. Costanzo, H. Berger, A. B. Kuzmenko, and A. F. Morpurgo, Nano Lett. **17**, 5719 (2017).
[49] J. Quereda, T. S. Ghiasi, J.-S. You, J. van den Brink, B. J. van Wees, and C. H. van der Wal, Nat. Commun. **9**, 3346 (2018).